PHYSICAL REVIEW RESEARCH **5**, L012023 (2023)

Letter

Role of spatiotemporal couplings in stimulated Raman side scattering

C. Zepter,[1,2,*] A. Seidel,[1,2] M. Zepf,[1,2,3] M. C. Kaluza,[1,2,3] and A. Sävert[2,3]
[1]*Institute of Optics and Quantum Electronics, Max-Wien-Platz 1, 07743 Jena, Germany*
[2]*Helmholtz-Institute Jena, Fröbelstieg 3, 07743 Jena, Germany*
[3]*GSI Helmholtzzentrum für Schwerionenforschung GmbH, Planckstraße 1, 64291 Darmstadt, Germany*

(Received 22 September 2021; revised 22 July 2022; accepted 15 December 2022; published 21 February 2023)

A high-intensity laser pulse propagating through underdense plasma is prone to parametric instabilities. We report on experiments investigating the influence of a pulse-front tilt (PFT), one of the most common spatiotemporal couplings in the laser focus, on stimulated Raman side scattering (SRSS). For a laser pulse exhibiting such a PFT, SRSS becomes asymmetric, varies as the pulse propagates through the plasma, and yields larger scattering angles than expected from traditional SRSS theory, indicating a correlation of the scattering with the PFT. We show that by including the propagation of a Gaussian laser pulse with a PFT in an analytical model, we can describe the observed asymmetric side scattering. Two-dimensional particle-in-cell simulations reproduce the observed scattering and the asymmetry induced by the PFT. A microscopic analysis of the simulation data shows that the sum of the angles from PFT and SRSS describe the observed side scattering.

DOI: 10.1103/PhysRevResearch.5.L012023

Over the last few years, the significance of spatiotemporal couplings (STCs) on laser-plasma physics has gained increasing attention. STCs describe the interdependence of spectral (or temporal) and spatial (or angular) coordinates of a laser pulse giving rise to various effects such as angular dispersion, spatial dispersion, or pulse-front tilt, affecting the laser's transverse extension and its temporal profile [1–6]. STCs have become a focus of research in simulations and experiments with numerous applications, including dephasingless wakefield acceleration, isolated attosecond pulse generation, or electron pulse steering [7–19]. However, the influence of STCs on some fundamental effects in plasma physics, namely parametric instabilities, also affecting the laser-plasma interaction, is an aspect whose importance has only been recognized in recent years.

One such parametric instability with several implications on modern laser-plasma physics [20–25] is stimulated Raman scattering (SRS) [26,27], which has been widely studied in both forward and backward geometries [28–32]. SRS is the resonant decay of an electromagnetic pump wave (angular frequency ω_0, wave number $\vec{k}_0$) into an electron plasma wave $(\omega, \vec{k})$ and a scattered electromagnetic wave $(\omega_0 \pm \omega, \vec{k}_0 \pm \vec{k})$. The beating of pump and scattered waves in turn enhances the plasma density modulation, which then further modulates the laser pulse's envelope, eventually resulting in an exponential growth of the instability. Compared to quasi-one-dimensional (1D) forward (SRFS) and backward scattering (SRBS), stimulated Raman side scattering (SRSS) is a two-dimensional (2D) effect, in which the wave is scattered under an angle θ to the pump's propagation direction. θ can be derived from the dispersion relation for which forward and back side scatter are indistinguishable and produce the same plasma wave number [33,34],

$$\sin\theta = \sqrt{\frac{2\,\omega_p}{\omega_0\sqrt{\gamma}}}, \tag{1}$$

with ω_p being the plasma frequency, $\gamma = \sqrt{1 + a_0^2/2}$ the electrons' Lorentz factor, and a_0 the normalized amplitude of the pump laser's vector potential.

As stated above, SRS is a parametric process involving the pump laser pulse and the background plasma. Hence, the growth of this instability requires a sufficiently long interaction time [28], which is governed by the pump pulse duration. When using state-of-the-art petawatt-class laser systems in underdense plasma experiments their pulse duration is usually too short. Furthermore, the growth of this instability is often limited due to the reduction of the on-axis electron density induced by ponderomotive displacement of the plasma electrons by the pump pulse. However, when the pump pulse exhibits STCs, the temporal and spatial dimensions of the formerly matched focal spot become larger, providing more favorable conditions for parametric instabilities to grow. In most applications the laser pulses have been assumed to have perfect Gaussian shapes and the effects of the peripheral parts of a real laser pulse have been neglected. Therefore it seems important to study the influence of STCs on the laser-plasma interaction, e.g., regarding effects such as SRSS, also with realistic (i.e., nonideal) laser pulse parameters.

In this Letter, we report on an experimental investigation of the influence of a PFT on SRSS during the propagation of a high-intensity (pump) laser pulse through underdense plasma. We show that a PFT can excite asymmetric SRSS. The measured scattering angle is up to 3.5 times larger than

---

[*] carola.zepter@uni-jena.de

expected from traditional 2D SRSS theory [Eq. (1)]. Furthermore, this angle varies as the laser propagates through the plasma. While the scattering angle follows the evolution and hence the orientation of the PFT angle when the pump pulse propagates through the focus, the phase-matching condition for SRSS changes in the same manner, leading to overall larger scattering angles. Our experimental findings are supported by 2D particle-in-cell (PIC) simulations, where a pump pulse with nonideal parameters as present in the experiments was implemented.

The experiments were performed with the JETi200 Ti:sapphire laser system at the Helmholtz-Institute Jena. Pump pulses (800 nm center wavelength, 2.8 J energy) were focused by an $f/25$ off-axis parabola into a supersonic helium gas jet generating a 3-mm-long underdense plasma with an electron density of $n_e = 1.1 \times 10^{19}$ cm^{-3}. The focal spot shape was elliptical (see Supplemental Material [35]) with $x_f = 46$ μm major and $y_f = 30$ μm minor full width at half maximum (FWHM) diameters and a measured Rayleigh length of $z_R = 1.2$ mm. The elliptical shape was caused by a spatial chirp with $\xi_0 = 0.73$ μm/nm due to nonparallel diffraction gratings in the pulse compressor. For these conditions, the shortest pulse duration was 20 fs (FWHM) and the highest intensity was $I_0 = 5.2 \times 10^{18}$ W/cm^2 (40% of the energy was contained in the FWHM area) leading to $a_0 = 1.5$. An acousto-optic programmable dispersive filter (AOPDF) could be used to add group delay dispersion (GDD) to the pump pulse ranging from -2650 to $+2650$ fs^2 in 400 fs^2 steps. A GDD of (0 ± 100) fs^2 gave the shortest pulse duration, and larger GDD values increased its duration and reduced a_0. Transverse shadowgrams of the interaction were taken using a synchronized 5-fs probe pulse and a high-resolution imaging system [36]. The pump pulse ionized the He gas and generated a plasma, which can be seen in three shadowgrams shown in Fig. 1. The pump's vacuum focus was positioned at $z = 0$ at the beginning of the gas-jet target. The lateral width of the laser-generated plasma was much wider ($\Delta x = 350 - 450$ μm) than for a Gaussian focal spot due to higher-order wavefront aberrations.

Figure 1 shows three shadowgrams taken with GDD of 0 and ±1050 fs^2 resulting in a global pulse duration of 20 and ∼150 fs, respectively, exhibiting three different behaviors. For 0 fs^2 no filaments are visible and the high-intensity part of the pump propagating to the right on the central axis excited a plasma wave with up to 30 periods [Fig. 1(b)]. For the orientation of our spatial chirp and a negative GDD, narrow filaments occur solely *above* the pump's propagation axis [Fig. 1(a)] and for a positive GDD they appear only *below* the axis [Fig. 1(c)]. Furthermore, for a fixed GDD value the angle α between the filaments and laser axis decreases with propagation of the pump, as indicated by the dashed arrows. These filaments are generated by radiation attributed to SRSS [37,38]. The scattered light is sufficiently intense to ionize helium outside the main-pulse region with the dashed arrows indicating the scattering direction. Tracing back the filaments to the laser axis ($x = 0$ μm), the origin of the scattering can be found.

In Fig. 2, a quantitative analysis of a systematic scan of the applied GDD is shown. For this analysis, the scattering angle α and the origin of the filament on the laser axis were measured along the brightness modulations of the ionization density perturbations. Error bars for the experimental data points are from the uncertainty of the fit to the scattering filaments and an error due to variation of k_0 from the focusing half-cone angle. The solid lines correspond to an analytical model (see below), and its error results from an uncertainty of the focus position $\pm z_R/4$ due to a possible wavefront jitter of the laser pulse [39]. Figure 2(a) shows $\alpha(z)$ for a GDD of $+1050$ fs^2 measured along the pump's propagation direction [cf. Fig. 1(c)], showing the decrease of $\alpha(z)$ with propagation. In addition to measuring the evolution of $\alpha(z)$ for one fixed GDD value, the variation of α with different GDD values both at the beginning and at the end of the plasma target was systematically studied [Fig. 2(b)]. The 10-shot averages of the maximum angles at the beginning (solid squares) and the minimum

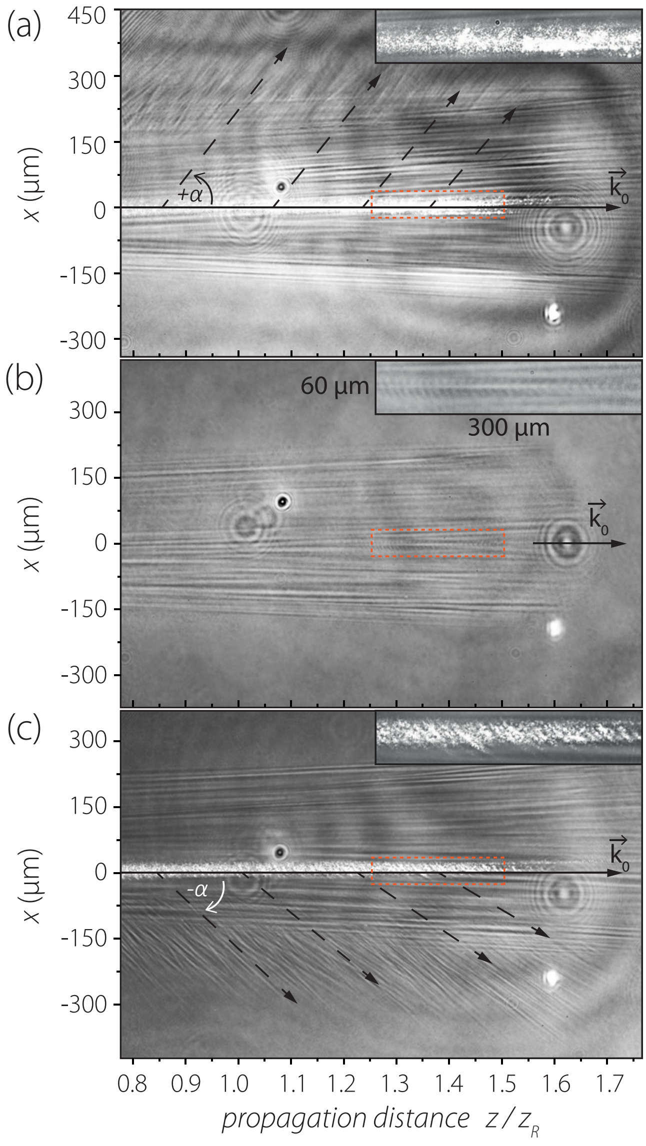

FIG. 1. Shadowgrams for (a) -1050 fs^2, (b) 0 fs^2, and (c) $+1050$ fs^2. $\vec{k}_0$ indicates the laser propagation axis, and the dashed arrows indicate the direction of side scattering. Diffraction rings are caused by dust on the optics. The insets shown in the upper right-hand corners are magnifications of the area in the orange rectangles.

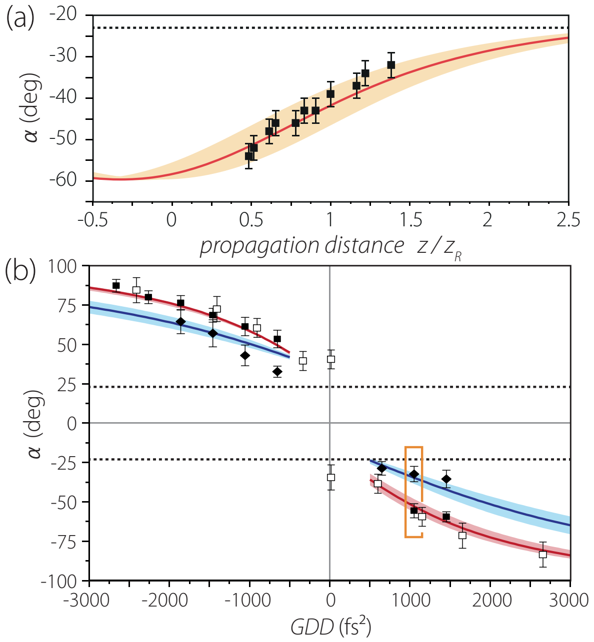

FIG. 2. (a) Side-scattering angle α as a function of z/z_R for $+1050$ fs^2. (b) Plot of the median angles measured at the beginning ($z_B = 0.4 z_R$, solid squares) and at the end ($z_E = 1.4 z_R$, solid diamonds) of the interaction over the applied GDD. The open squares represent the most dominant scattering angles from simulations. The orange rectangle corresponds to the data shown in (a). The solid lines in (a) and (b) are given by an analytical model explained below.

angles at the end of the interaction (open squares) are shown for different GDD values. For |GDD| < 500 fs^2 no side scattering could be detected. For increasing absolute values of GDD, however, scattering was visible and we found an overall increase of $|\alpha|$. Again, the decrease of $|\alpha(z)|$ with propagation z for each value of GDD and the scattering asymmetry depending on the sign of the GDD can be seen in Fig. 2(b).

Since, apart from relativistic corrections, the SRSS angle θ solely depends on ω_p and ω_0, symmetric and propagation-independent SRSS under an angle of $\theta = \pm 23^\circ$ would be expected for our experimental parameters (black dashed lines in Fig. 2). In addition, the longer pulse duration due to added GDD reduces the peak intensity below the relativistic limit, making relativistic corrections in Eq. (1) negligible. This indicates that the mechanisms responsible for the observed scattering cannot be traditional SRSS as described by Eq. (1) since neither the absolute values, nor the GDD-dependent asymmetry, nor the change of the scattering angle with propagation are explained by this. In Ref. [37] the latter was attributed to intensity amplification, but this is unlikely for our conditions.

So far, imperfections in the laser focus have not been considered in the description of similar scattering processes occurring in high-intensity laser-matter interactions. STCs being such an imperfection, can, as described above, intentionally or unintentionally be induced by a misalignment of the diffraction gratings in the stretcher-compressor combination, which leads to angular dispersion resulting in a PFT of the unfocused beam [40–42]. Such a PFT creates a spatiotemporal intensity envelope of the pump pulse tilted with respect to the pulse's phase fronts, the latter being perpendicular to the pulse's propagation direction. Focusing these pulses results in a laterally dispersed beam, or a spatial chirp in the focal plane. While there is no PFT in the focus itself, the tilt direction changes around the focal plane. However, additionally applying GDD to the pulse in combination with such a spatial chirp results in a controllable PFT also in the focus. Akturk *et al.* [43] have studied the PFT for a *collimated* beam exhibiting STCs. Here, we consider a more general approach, examining a Gaussian beam propagating through focus with a linear spatial chirp $\xi_0 = dx_0/d\omega$ in one transverse direction, a linear angular dispersion $\beta_0 = d\Theta_0/d\omega$, and a GDD value φ. x_0 is the transverse position of a ω component, ω is the offset to ω_0, and Θ_0 is this component's propagation angle. Neglecting propagation effects before focus, the electric field at $z = 0$ can be expressed as [43]

$$E(x, 0, \omega) = E_0 \exp\left(\frac{-\omega^2 \tau_0^2}{4}\right) \exp(-i k_0 \beta_0 \omega x) \times \exp\left(\frac{-i k_0 (x - \xi_0 \omega)^2}{2 i z_R}\right) \exp\left(-i \frac{\varphi}{2} \omega^2\right), \tag{2}$$

where τ_0 and w_0 are the rms pulse duration and beam waist of the undistorted beam, respectively. We concentrate on distortions in the x direction only. After propagating the beam to an arbitrary z position using the Huygens-Fresnel integral in one dimension, an inverse Fourier transform was performed to obtain the field in the temporal domain. By decoupling z_R and w_0 to obtain a modeling closer to the real beam, the vacuum PFT angle ψ between the phase and intensity fronts at a distance z from focus is given by

$$\begin{aligned}\tan\psi &= \big[-c k_0 \xi_0 w_0^2 \tau_0^2 z + c\big\{(4\varphi(\xi_0 + \beta_0 z) \\ &\quad + \beta_0 k_0\big[w_0^2 \tau_0^2 + 4\xi_0(\xi_0 + \beta_0 z)\big]\big\} z_R^2\big] \\ &\quad \times\big[4(\xi_0 + \beta_0 z)^2 z_R^2 + w_0^2 \tau_0^2 \big(z^2 + z_R^2\big)\big]^{-1} \\ &= \left[k_0 \beta(z) + \frac{\xi(z)}{\xi(z)^2 + \frac{w_0^2\, \tau_0^2 (z^2 + z_R^2)}{4\, z_R^2}} \varphi_{\text{eff}}(z)\right] c,\end{aligned} \tag{3}$$

with β, ξ, φ_{eff}, and c being the propagation-dependent angular chirp (AC), spatial chirp (SC), temporal chirp (TC), and vacuum speed of light, respectively. The expression describing the PFT consists of two terms: A first term, which links AC to PFT, and a second, which describes the PFT as a combination of SC and TC. A more detailed discussion of Eq. (3) can be found in the Supplemental Material [35]. Assuming a collimated beam ($z_R \to \infty$), Eq. (3) is equivalent to the results in Ref. [43]. Inserting the experimental values—rms duration $\tau_0 = 17$ fs (20 fs FWHM), beam waist $w_0 = 26$ µm, GDD of $+1050$ fs^2, $\xi_0 = 0.73$ µm/nm, and $\beta_0 = -5.37$ µrad/nm—into Eq. (3) shows that $|\psi|$ increases approaching the focal plane until reaching its maximum at $z \approx 0$ before decreasing again (see Supplemental Material [35]). Comparing the measured scattering angles in Fig. 2(a) and Eq. (3) shows that they follow the same curve and differ only by an angular offset of about $22.6^\circ \pm 3.0^\circ$, comparable to the SRSS angle for our parameters, $\theta = 23^\circ$. This indicates that the total scattering

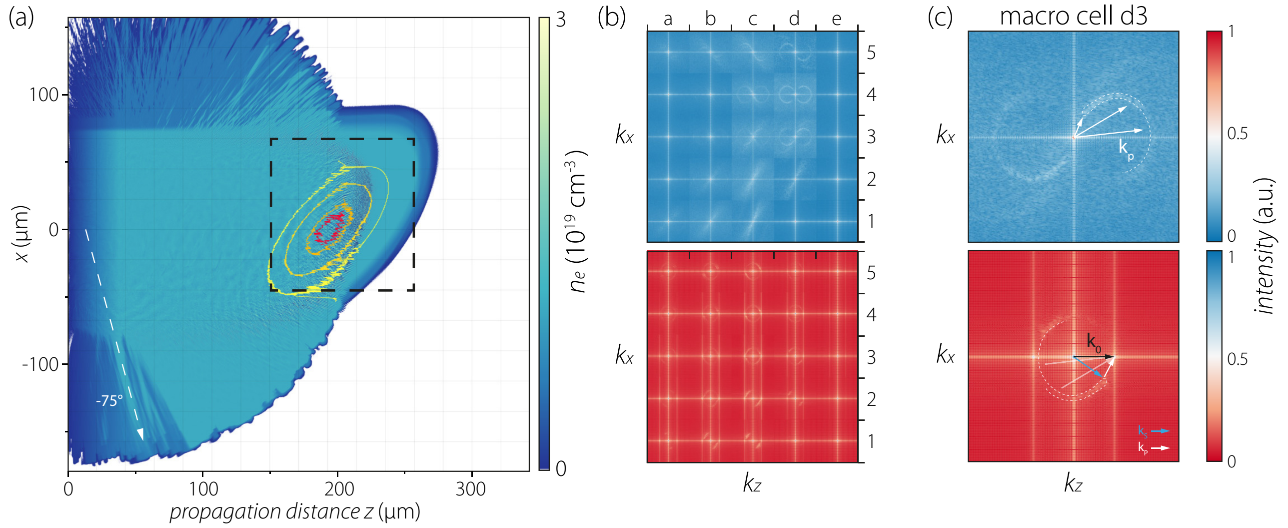

FIG. 3. (a) Simulated electron density profile of a laser pulse with a PFT of -33° after 200 μm propagation overlaid with the laser's intensity isocontours. (b) The black dashed region was divided into 5×5 macrocells and for each cell a 2D FT was performed yielding spatially resolved information about the k vectors present in the plasma (blue) and E_y (red). The vertical lines in the k diagrams of E_y are FT artifacts marking the position of the pump. (c) Exemplary k-vector analysis of macrocell d3 showing phase matching of the wave vectors of the pump ($\vec{k}_0$), the scattered light ($\vec{k}_s$), and the plasma wave ($\vec{k}_p$) as one can find a signal in both graphs, such that $\vec{k}_s + \vec{k}_p = \vec{k}_0$. For better visualization the fourth root of the signal is plotted in (b) and (c).

angle α can be seen as a combination of the PFT angle ψ and the SRSS angle θ,

$$\alpha = \psi + \operatorname{sgn}(\psi)\,\theta. \tag{4}$$

Figure 2 shows that this model not only describes the change of α for one GDD value during propagation but also the behavior of α for a wide range of GDDs at the beginning and end of the interaction, as it lies well within the error range of the measured data.

Systematic 2D PIC simulations including ionization were performed with the code SMILEI [44] to investigate the microscopic behavior of SRSS. A simulation box with a dimension of 342 μm × 359 μm with $10\,752 \times 2816$ cells and 64 particles per cell was used. A laser pulse modeled by the Fourier transform of Eq. (2) containing all the STCs identified in the experiment with an out-of-plane polarization (E_y) was focused in He gas with an atomic density $n_0 = 0.55 \times 10^{19}$ cm^{-3}. By varying the GDD the PFT was changed, resulting in angles of $+3^\circ$, -16°, -33°, -44°, and -58°. The peak intensity was set to $a_0 = 2.5$ for -33° and adapted to the respective PFT.

Figure 3(a) shows an exemplary snapshot of the simulation with the pump's intensity contours, and the plasma electron density. The PFT of the pump manifests itself in the tilted intensity isocontours and leads to a tilted ionization front. Above and below the laser axis an asymmetry in the electron density can be seen caused by the asymmetric side scattering from the laser pulse. The downward scattering is more pronounced compared to the upward direction. For the downward direction, scattering angles up to -75° appear, clearly exceeding the SRSS angle from Eq. (1).

To show phase matching of the Raman scattering process, the k vectors of the E_y field and the plasma were analyzed in a spatially resolved manner. Here, the simulation box was divided into macrocells with a side length of 22 μm and 2D Fourier transformations (FTs) of E_y and the plasma density were carried out [cf. Figs. 3(b) and 3(c)]. The bright lines for $k_x = 0$ and $k_z = 0$ are artifacts from the FT. The strong signal on the z axis of the FT corresponds to $\vec{k}_0$ of the pump. The presence of modes with $k_x^2 + k_z^2 = |\vec{k}_s|^2$, i.e., modes with the same frequency, is indicative of SRSS. This implies for the Stokes component with $|\vec{k}_s| \sim \omega_s = (\omega_0 - \omega_p)$ that it lies on a circle around the origin with radius $|\vec{k}_s| < |\vec{k}_0|$ [Fig. 3(c)] [33]. Note that the scattered light has a finite bandwidth, which is a direct consequence of the pump's bandwidth. The plasma wave's k vectors necessary for the Stokes scattering of the pump are therefore also located on a circle with radius $|\vec{k}_s|$ but with an offset of ω_p/c to the origin. Comparing the wave vectors present in the plasma density and in E_y [Fig. 3(c)], we observe phase matching of $\vec{k}_0$, $\vec{k}_s$, and $\vec{k}_p$ showing that the origin of the scattered light ionizing the neutral gas outside the pump's ionization channel is indeed Raman scattering.

The FTs also give insight into the microscopic mechanisms leading to the apparent scattering asymmetry. In Fig. 3(b), it can be seen that in the region of the laser front (macrocell d4), plasma k vectors of the Raman instability are present in almost every direction, also leading to light scattering in every direction. Since the front of the pulse is tilted the leading edge correlates with the top of the pulse. As a result, light from an earlier point in time, which was scattered downward, can overlap with the lower part of the pump pulse while propagating. This enables pump and scattered light to beat and thus to enhance the growth of the Raman instability in a downward direction. The upward scattered light, on the other hand, has less overlap with the pump, resulting in less scattering in the upward direction, which leads to the observed asymmetry.

To deduce the visible scattering angles for different PFTs, an FT of E_y of the entire simulation box was made for all simulation runs after 115 μm propagation. This (short)

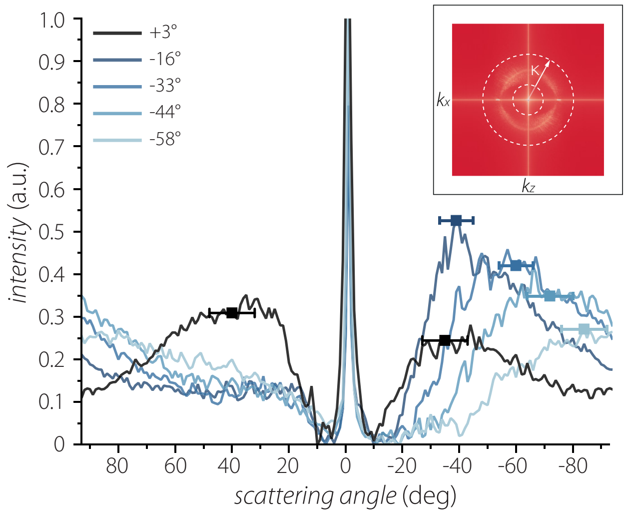

FIG. 4. Angular distribution of the scattered radiation after a radial integration of the signal from the FT of E_y of the whole image for five different angles of PFT after 115 μm of propagation. Note that negative scattering angles correspond to downward scattering. The inset exemplarily shows the FT of E_y for a pump pulse with a PFT of -33°.

propagation length was chosen to ensure that (i) the PFT does not differ from the calculated vacuum PFT angle and (ii) to minimize small-angle scattered light contributions from earlier times in the interaction. The resulting k diagram shows all directions and magnitudes of the transverse E_y field present at this time step, as shown in the inset of Fig. 4. This signal was integrated in a radial direction over the range $0.5|k_0| \leqslant \kappa \leqslant 1.5|k_0|$ for each scattering direction (i.e., between -90° and $+90^\circ$) as shown in Fig. 4. The strongest side-scattering angles were found by fitting the data with a multiple peak fit and identifying the maximum of the envelope function. The error bars were determined by determining the angle spread of 98% of the maximum values. We find that the strongest scattering angle increases with increasing PFT angle as observed in the experiment.

To compare simulation and experimental results Eq. (3) was used to convert the PFT angles to the corresponding GDD for $z = 0.4z_R$. It can be seen in Fig. 2(b) that, except for very small values of GDD, the simulation results very well reproduce the analytical model and the experimental data, i.e., the scattering asymmetry and their increase with increasing PFT values.

In summary, we have presented experimental measurements of the influence of STCs on SRSS in underdense plasmas. The scattering angle strongly depends on the pump's pulse-front tilt and the final scattering angle can be expressed as the sum of the PFT angle and SRSS angle as derived from 2D theory, indicating a rotation of the frame of reference of the scattering process. The simulations could also reveal the underlying mechanism, showing that phase matching is indeed possible for a variety of scattering angles. However, only those modes experiencing a sufficient spatiotemporal overlap with the pump will grow stronger. Additional simulations not shown here indicate that this mechanism is present over a wide range of plasma densities down to 10^{17} cm^{-3}, which is the optimum density for 10 GeV acceleration stages, e.g., for future laser-based particle colliders [45]. Our results further emphasize the relevance of STCs on the dynamics of laser-plasma interactions and laser-particle accelerators especially when employing next-generation multi-PW-laser systems. They are particularly prone to STCs such as PFT, which need to be precisely controlled and described in the future.

ACKNOWLEDGMENTS

The authors thank G. Schäfer for operating the JETi200-laser system and D. Seipt, M. Hornung, and S. Tietze for helpful discussions. This work was supported by the Bundesministerium für Bildung und Forschung (BMBF) Grants No. 05K19SJC, No. 05K19SJB, No. 05K22SJA, and No. 05K22SJB. The research leading to the presented results received additional funding from the European Regional Development Fund and the State of Thuringia (Contract No. 2019 FGI 0013).

---

[1] S. Akturk, X. Gu, P. Gabolde, and R. Trebino, The general theory of first-order spatio-temporal distortions of Gaussian pulses and beams, Opt. Express **13**, 8642 (2005).

[2] S. W. Jolly, O. Gobert, and F. Quéré, Spatio-temporal characterization of ultrashort laser beams: A tutorial, J. Opt. **22**, 103501 (2020).

[3] O. E. Martinez, Grating and prism compressors in the case of finite beam size, J. Opt. Soc. Am. B **3**, 929 (1986).

[4] G. Pretzler, A. Kasper, and K. J. Witte, Angular chirp and tilted light pulses in CPA lasers, Appl. Phys. B: Lasers Opt. **70**, 1 (2000).

[5] O. E. Martinez, J. P. Gordon, and R. L. Fork, Negative group-velocity dispersion using refraction, J. Opt. Soc. Am. A **1**, 1003 (1984).

[6] K. Osvay, A. P. Kovacs, Z. Heiner, G. Kurdi, J. Klebniczki, and M. Csatari, Angular dispersion and temporal change of femtosecond pulses from misaligned pulse compressors, IEEE J. Sel. Top. Quantum Electron. **10**, 213 (2004).

[7] J. Wheeler, A. Borot, S. Monchocé, H. Vincenti, A. Ricci, A. Malvache, R. Lopez-Martens, and F. Quere, Attosecond lighthouses from plasma mirrors, Nat. Photonics **6**, 829 (2012).

[8] D. H. Froula, J. P. Palastro, D. Turnbull, A. Davies, L. Nguyen, A. Howard, D. Ramsey, P. Franke, S.-W. Bahk, I. A. Begishev, R. Boni, J. Bromage, S. Bucht, R. K. Follett, D. Haberberger, G. W. Jenkins, J. Katz, T. J. Kessler, J. L. Shaw, and J. Vieira, Flying focus: Spatial and temporal control of intensity for laser-based applications, Phys. Plasmas **26**, 032109 (2019).

[9] C. Caizergues, S. Smartsev, V. Malka, and C. Thaury, Phase-locked laser-wakefield electron acceleration, Nat. Photonics **14**, 475 (2020).

[10] J. P. Palastro, J. L. Shaw, P. Franke, D. Ramsey, T. T. Simpson, and D. H. Froula, Dephasingless Laser Wakefield Acceleration, Phys. Rev. Lett. **124**, 134802 (2020).

[11] D. Turnbull, S. Bucht, A. Davies, D. Haberberger, T. Kessler, J. L. Shaw, and D. H. Froula, Raman Amplification with a Flying Focus, Phys. Rev. Lett. **120**, 024801 (2018).

[12] A. Popp, J. Vieira, J. Osterhoff, Z. Major, R. Hörlein, M. Fuchs, R. Weingartner, T. P. Rowlands-Rees, M. Marti, R. A. Fonseca, S. F. Martins, L. O. Silva, S. M. Hooker, F. Krausz, F. Grüner, and S. Karsch, All-Optical Steering of Laser-Wakefield-Accelerated Electron Beams, Phys. Rev. Lett. **105**, 215001 (2010).

[13] M. Schnell, A. Sävert, I. Uschmann, M. Reuter, M. Nicolai, T. Kämpfer, B. Landgraf, O. Jäckel, O. Jansen, A. Pukhov, M. Kaluza, and C. Spielmann, Optical control of hard X-ray polarization by electron injection in a laser wakefield accelerator, Nat. Commun. **4**, 2421 (2013).

[14] M. C. Kaluza, S. P. D. Mangles, A. G. R. Thomas, Z. Najmudin, A. E. Dangor, C. D. Murphy, J. L. Collier, E. J. Divall, P. S. Foster, C. J. Hooker, A. J. Langley, J. Smith, and K. Krushelnick, Observation of a Long-Wavelength Hosing Modulation of a High-Intensity Laser Pulse in Underdense Plasma, Phys. Rev. Lett. **105**, 095003 (2010).

[15] P. Sprangle, J. Krall, and E. Esarey, Hose-Modulation Instability of Laser Pulses in Plasmas, Phys. Rev. Lett. **73**, 3544 (1994).

[16] M. Thévenet, D. E. Mittelberger, K. Nakamura, R. Lehe, C. B. Schroeder, J.-L. Vay, E. Esarey, and W. P. Leemans, Pulse front tilt steering in laser plasma accelerators, Phys. Rev. Accel. Beams **22**, 071301 (2019).

[17] D. E. Mittelberger, M. Thévenet, K. Nakamura, A. J. Gonsalves, C. Benedetti, J. Daniels, S. Steinke, R. Lehe, J.-L. Vay, C. B. Schroeder, E. Esarey, and W. P. Leemans, Laser and electron deflection from transverse asymmetries in laser-plasma accelerators, Phys. Rev. E **100**, 063208 (2019).

[18] S. Hüller, G. Raj, M. Luo, W. Rozmus, and D. Pesme, Crossed beam energy transfer between optically smoothed laser beams in inhomogeneous plasmas, Philos. Trans. R. Soc. A **378**, 20200038 (2020).

[19] R. L. Berger, E. Lefebvre, A. B. Langdon, J. E. Rothenberg, C. H. Still, and E. A. Williams, Stimulated Raman and Brillouin scattering of polarization-smoothed and temporally smoothed laser beams, Phys. Plasmas **6**, 1043 (1999).

[20] Z. Najmudin, K. Krushelnick, E. L. Clark, S. P. D. Mangles, B. Walton, A. E. Dangor, S. Fritzler, V. Malka, E. Lefebvre, D. Gordon, F. S. Tsung, and C. Joshi, Self-modulated wakefield and forced laser wakefield acceleration of electrons, Phys. Plasmas **10**, 2071 (2003).

[21] B. Hidding, K.-U. Amthor, B. Liesfeld, H. Schwoerer, S. Karsch, M. Geissler, L. Veisz, K. Schmid, J. G. Gallacher, S. P. Jamison, D. Jaroszynski, G. Pretzler, and R. Sauerbrey, Generation of Quasimonoenergetic Electron Bunches with 80-fs Laser Pulses, Phys. Rev. Lett. **96**, 105004 (2006).

[22] N. Lemos, J. L. Martins, F. S. Tsung, J. L. Shaw, K. A. Marsh, F. Albert, B. B. Pollock, and C. Joshi, Self-modulated laser wakefield accelerators as x-ray sources, Plasma Phys. Controlled Fusion **58**, 034018 (2016).

[23] G. Vieux, S. Cipiccia, D. Grant, N. Lemos, P. Grant, C. Ciocarlan, B. Ersfeld, M. S. Hur, P. Lepipas, G. Manahan, G. Raj, D. Gil, A. Subiel, G. Welsh, S. Wiggins, S. Yoffe, J. Farmer, C. Aniculaesei, E. Brunetti, and D. Jaroszynski, An ultra-high gain and efficient amplifier based on Raman amplification in plasma, Sci. Rep. **7**, 2399 (2017).

[24] G. Vieux, E. Brunetti, S. Cipiccia, B. Eliasson, B. Ersfeld, J. P. Farmer, M. S. Hur, N. Lemos, G. H. Welsh, S. M. Wiggins, X. Yang, S. R. Yoffe, J. M. Dias, and D. A. Jaroszynski, Towards a high efficiency amplifier based on Raman amplification, Plasma Phys. Controlled Fusion **62**, 014018 (2020).

[25] R. Trines, E. P. Alves, E. Webb, J. Vieira, F. Fiuza, R. Fonseca, L. Silva, R. Cairns, and R. Bingham, New criteria for efficient Raman and Brillouin amplification of laser beams in plasma, Sci. Rep. **10**, 19875 (2020).

[26] T. M. Antonsen and P. Mora, Self-Focusing and Raman Scattering of Laser Pulses in Tenuous Plasmas, Phys. Rev. Lett. **69**, 2204 (1992).

[27] C. S. Liu, M. N. Rosenbluth, and R. B. White, Parametric Scattering Instabilities in Inhomogeneous Plasmas, Phys. Rev. Lett. **31**, 697 (1973).

[28] J. F. Drake, P. K. Kaw, Y. C. Lee, G. Schmidt, C. S. Liu, and M. N. Rosenbluth, Parametric instabilities of electromagnetic waves in plasmas, Phys. Fluids **17**, 778 (1974).

[29] D. W. Forslund, J. M. Kindel, and E. L. Lindman, Theory of stimulated scattering processes in laser-irradiated plasmas, Phys. Fluids **18**, 1002 (1975).

[30] G. Shvets, J. S. Wurtele, and B. A. Shadwick, Analysis and simulation of Raman backscatter in underdense plasmas, Phys. Plasmas **4**, 1872 (1997).

[31] W. B. Mori, C. D. Decker, D. E. Hinkel, and T. Katsouleas, Raman Forward Scattering of Short-Pulse High-Intensity Lasers, Phys. Rev. Lett. **72**, 1482 (1994).

[32] C. B. Schroeder, E. Esarey, B. A. Shadwick, and W. P. Leemans, Raman forward scattering of chirped laser pulses, Phys. Plasmas **10**, 285 (2003).

[33] W. B. Mori, C. Joshi, J. M. Dawson, D. W. Forslund, and J. M. Kindel, Two Dimensional Simulations of Intense Laser Irradiation of Underdense Plasmas, in *Laser Interaction and Related Plasma Phenomena*, edited by H. Hora and G. H. Miley (Springer, Boston, MA, 1986), Vol. 7, pp. 767–779.

[34] D. W. Forslund, J. M. Kindel, W. B. Mori, C. Joshi, and J. M. Dawson, Two-Dimensional Simulations of Single-Frequency and Beat-Wave Laser-Plasma Heating, Phys. Rev. Lett. **54**, 558 (1985).

[35] See Supplemental Material at http://link.aps.org/supplemental/10.1103/PhysRevResearch.5.L012023 for a more detailed description of the focal spot analysis and a detailed description and discussion of a focused laser pulse exhibiting pulse front tilt due to spatiotemporal couplings.

[36] M. B. Schwab, A. Sävert, O. Jäckel, J. Polz, M. Schnell, T. Rinck, L. Veisz, M. Möller, P. Hansinger, G. G. Paulus, and M. C. Kaluza, Few-cycle optical probe-pulse for investigation of relativistic laser-plasma interactions, Appl. Phys. Lett. **103**, 191118 (2013).

[37] T. Matsuoka, C. McGuffey, P. G. Cummings, Y. Horovitz, F. Dollar, V. Chvykov, G. Kalintchenko, P. Rousseau, V. Yanovsky, S. S. Bulanov, A. G. R. Thomas, A. Maksimchuk, and K. Krushelnick, Stimulated Raman Side Scattering in Laser Wakefield Acceleration, Phys. Rev. Lett. **105**, 034801 (2010).

[38] K. Krushelnick, A. E. Dangor, M. Kaluza, S. P. D. Mangles, C. D. Murphy, Z. Najmudin, and A. G. R. Thomas, Observation of anomalous side-scattering in laser wakefield accelerators, Laser Part. Beams **36**, 391 (2018).

[39] A. R. Maier, N. M. Delbos, T. Eichner, L. Hübner, S. Jalas, L. Jeppe, S. W. Jolly, M. Kirchen, V. Leroux, P. Messner, M. Schnepp, M. Trunk, P. A. Walker, C. Werle, and P. Winkler, Decoding Sources of Energy Variability in a Laser-Plasma Accelerator, Phys. Rev. X **10**, 031039 (2020).

[40] O. E. Martinez, Pulse distortions in tilted pulse schemes for ultrashort pulses, Opt. Commun. **59**, 229 (1986).

[41] Z. Bor, B. Racz, G. Szabo, M. Hilbert, and H. A. Hazim, Femtosecond pulse front tilt caused by angular dispersion, Opt. Eng. **32**, 2501 (1993).

[42] J. Hebling, Derivation of the pulse front tilt caused by angular dispersion, Opt. Quantum Electron. **28**, 1759 (1996).

[43] S. Akturk, X. Gu, E. Zeek, and R. Trebino, Pulse-front tilt caused by spatial and temporal chirp, Opt. Express **12**, 4399 (2004).

[44] J. Derouillat, A. Beck, F. Pérez, T. Vinci, M. Chiaramello, A. Grassi, M. Flé, G. Bouchard, I. Plotnikov, N. Aunai, J. Dargent, C. Riconda, and M. Grech, SMILEI: A collaborative, open-source, multi-purpose particle-in-cell code for plasma simulation, Comput. Phys. Commun. **222**, 351 (2018).

[45] A. J. Gonsalves, K. Nakamura, J. Daniels, C. Benedetti, C. Pieronek, T. C. H. de Raadt, S. Steinke, J. H. Bin, S. S. Bulanov, J. van Tilborg, C. G. R. Geddes, C. B. Schroeder, C. Tóth, E. Esarey, K. Swanson, L. Fan-Chiang, G. Bagdasarov, N. Bobrova, V. Gasilov, G. Korn *et al.*, Petawatt Laser Guiding and Electron Beam Acceleration to 8 GeV in a Laser-Heated Capillary Discharge Waveguide, Phys. Rev. Lett. **122**, 084801 (2019).